Journal of Chemical&Engineering Data

pubs.acs.org/jced Article

Data-Driven Optimization of Carbon Electrodes for Aqueous Supercapacitors

Runtong Pan, Mengyang Gu, and Jianzhong Wu*

Cite This: https://doi.org/10.1021/acs.jced.4c00071 Read Online

ACCESS | Metrics & More | Article Recommendations | Supporting Information

ABSTRACT: Doping carbon electrodes with heteroatoms such as nitrogen and oxygen proves effective in improving the performance of aqueous supercapacitors. However, the optimal conditions of N/O doping remain elusive due to the complexity of the porous structure and electrochemical behavior. While physics-based models face challenges in capturing the pseudocapacitance effects, direct empirical correlation of the capacitance with machine-learning (ML) methods may lead to erroneous predictions. In this work, we introduce a Gaussian process regression (GPR) method using a physical model as prior knowledge to limit the coupling effects of different input parameters. The physics-informed GPR proves effective in characterizing the capacitive behavior of N/O-codoped carbon electrodes in both 6 M KOH and 1 M H_2SO_4 aqueous solutions. Our machine-learning model suggests that the performance of aqueous supercapacitors can be maximized under acidic conditions by enhancing both the mesopore surface area and the O/N doping ratio of carbon electrodes.

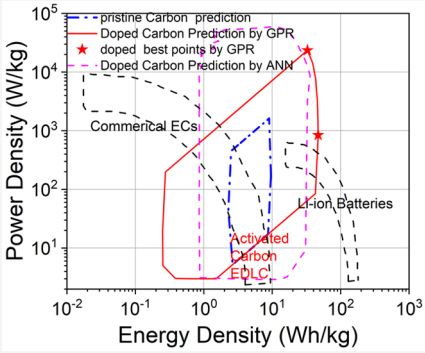

1. INTRODUCTION

Supercapacitors have attracted great interest over the past few decades for their applications in rapid energy storage devices, such as regenerative braking systems in vehicles and power levelers for electronics. In comparison with alternative means of energy storage, supercapacitors have the advantages of high-power density and cycling stability, allowing them to bridge the gap between dielectric capacitors and electrochemical batteries in terms of energy density and power delivery. The charging mechanisms of supercapacitors are mostly associated with electric double layer (EDL) capacitance and/or electrochemical pseudocapacitance.[1] The EDL capacitance is associated with electrostatic polarization at the electrolyte−electrode interface. Electrochemical pseudocapacitance arises from reversible faradaic redox reactions or the intercalation of ionic species into the micropores of electrodes.[2−4] For supercapacitors made of carbon electrodes and aqueous electrolytes, both pseudocapacitance and EDL capacitance contribute to energy storage, making them a popular choice for practical applications.

Diverse electrode materials, including porous carbons, metal oxides/nitrides/carbides, and conductive polymers, have been investigated for optimizing the energy and power density of aqueous supercapacitors.[5,6] From a practical perspective, porous carbons remain a preferred choice due to their high porosity, large specific surface area, good conductivity, long-term cycle stability, and low production cost.[2] Given that the capacitance of a carbon electrode primarily arises from the EDL capacitance, we can enhance the device performance by increasing the surface area available for the adsorption of ionic species. However, the specific capacitance reaches a plateau when the electrode surface area is larger than about 1500 m^2/g,[7] suggesting that the EDL capacitance is also influenced by the pore structures. While micropores (pore diameter $d < 2$ nm) usually yield a higher specific surface area than both mesopores (2 nm $< d <$ 50 nm) and macropores ($d >$ 50 nm), increasing the micropore surface area would also reduce the electrical conductivity, interfere with ion adsorption in neighboring pores, and restrict ion accessibility, making micropores less significant in contributing to the EDL capacitance.[8−11] Inconsistent experimental results were reported when the pore sizes were comparable to those of the ionic species, yet theoretical investigations are not fully conclusive due to the complexities in the characterization of the pore structure and surface conditions of electrode materials.[12−14]

Although ultrahigh EDL capacitance, up to 348 F/g, has been reported for aqueous supercapacitors,[15] the specific capacitance can be further improved by introducing heteroatoms into pristine carbon electrodes. Common strategies include doping porous carbon with electroactive elements such as O, N, S, and P, using carbide-derived carbon with transition-metal additives, and coating the electrode surface with metal oxides.[2,16] The further enhancement of supercapacitor

Special Issue: In Honor of Xiaohua Lu

Received: February 4, 2024
Revised: April 6, 2024
Accepted: April 12, 2024

Table 1. Comparison of Common ML Methods for Predicting Supercapacitor Behavior

ML Algorithm	Advantages	Disadvantages
Artificial neural network (ANN, including multilayer perceptron (MLP))	Effective nonlinear modeling, good generalizability as universal functional estimation, implicit feature selection	Prone to overfitting, hard to tune, a large number of hyperparameters
Support vector machine (SVM) and	Effective in high dimensions, robust to outliers,	Slow, tricky in kernel selection
Decision trees (including random forest (RF), regression trees (RT), etc.)	good performance on imbalanced data, not prone to overfitting, low impact of outlier, easy to parallelize	High computational cost, low interpretability, low efficiency in nonlinearity
Generalized linear regression (GLM)	Easy to understand and use, high interpretability	Low accuracy, easily impacted by outliers, prone to overfitting
K-Nearest neighbor (KNN)	Simple to implement, nonparametric	Sensitive to outliers, poor efficiency with large data sets, hard to tune
Gaussian process (GP)	High accuracy, high learning efficiency, reliable uncertainty quantification, effective in high dimensions, good generalizability as universal functional estimation	High computational cost for large data sets, tricky in kernel selection
Gradient boosting (such as XGBoost)	Usually used with decision trees, fast, easy to parallelize	Prone to overfitting if applied alone (not in a decision tree), low interpretability

performance stems from various factors. First, heteroatom doping improves the electrical conductivity of the carbon electrodes and electrolyte wettability, thus facilitating better ion accessibility of micropores and increasing the EDL capacitance.[2,16,17] Second, doping with heteroatoms expands the electronic density of states (DOS) of the carbon material, leading to additional contributions due to quantum capacitance.[17−20] Finally, heteroatoms catalyze reversible redox reactions and/or more electrosorption of the electrolyte ions.[17,18] For example, capacitors made with graphene oxide (GO), reduced graphene oxide (rGO), or nitrogen-doped carbon nanotubes exhibit strong pseudocapacitance because of the redox reactions of the oxygen- or nitrogen-containing functional groups on the electrode surface.[21−23] Besides, heteroatom doping can improve the specific surface areas of carbon materials. The theoretical upper limit for the specific surface area of pristine carbonaceous materials was 2630 m^2/g, estimated from the infinite single-layer prefect graphene.[24] Introducing heteroatoms allows for the exposure of ring faces and edges of the carbon material, thus significantly increasing the possible surface area.[25] While the capacitance of pristine carbon reaches a plateau at about 1500 m^2/g, the capacitance of doped carbon electrodes continues to increase with the specific surface area, reaching 4000 m^2/g.[26]

Physics-based models have been previously utilized to unravel various mechanisms of enhanced capacitance due to heteroatom doping.[17,28,29] For example, *ab initio* methods has been utilized to predict pseudocapacitances of certain chemically simple doped carbons, such as GO[21] and pyrrolic nitrogen (N-5)-doped carbon nanotubes.[30] In general, the quantum chemistry methods are extremely computationally costly and not practical for systems with more than 1,000 atoms. A comprehensive description of the doping effects has yet to be developed, especially concerning the pseudocapacitance of mixed heteroatom-doped carbons and the geometric effects of doping. In practice, supercapacitance performance is often assessed under conditions remote from the thermodynamic equilibrium. In contrast, *ab initio* calculations mostly address the equilibrium properties at small scale, providing little information about the dynamic behavior of the energy-storage device because of the ultrahigh computational cost of time-dependent models. As a result, existing physics-based models face challenges in providing quantitative predictions of capacitance under the operational conditions of practical devices.

In addition to physics-based modeling, machine learning (ML) methods have also been introduced to predict the performance of aqueous supercapacitors for energy storage.[17,27] The data-driven approach allows us to establish quantitative correlations between the characteristics of the electrode materials and the *in operando* performance based on extensive experimental data. Table 1 summarizes the advantages and disadvantages of commonly used ML methods for capacitance prediction. Previously, different ML methods, including ANN, SVM, RT, and GLM models, have been applied to quantitatively predict the EDL capacitance based on the physicochemical features of carbon materials, such as specific surface area, pore volume, and doping atoms, under the same low-level charging−discharging rates.[31,32] ANN has also been used to describe the synergetic effect of N/O doping on supercapacitor performance[26] as well as to model the EDL capacitance in terms of the physical features of carbon materials and the charging current density. In our previous studies,[31,32] we tested multiple ML methods to predict the overall capacitance of both pristine carbon and N/O-codoped carbon electrodes in response to the changing scan rate of cyclic voltammetry. We found that ANN models show the best performance in capacitance prediction,[32−35] but its erroneous behavior limits its application to materials with high mesopore surface area.[36] ML methods can also be used to find the relative importance of the supercapacitor characteristics to their capacitance behavior by applying sensitivity analysis methods such as SHAP or Sobol indices. It is often observed that the specific surface area (SSA), pore volume (PV), and oxygen ratio are among the most important parameters representing the properties of carbon electrodes.[34,37,38] The ML predictions offer valuable insights into the synthesis of better carbon materials, help to identify critical features, optimize reaction conditions, and predict and optimize the cycle life, thereby facilitating advancements in carbon material synthesis.[26,39,40] Conversely, new experimental data can be leveraged to refine and enhance the predictive accuracy of ML models.

While data-driven methods are able to make valuable predictions of supercapacitance performance, their pitfalls have also been well recognized, such as low robustness, challenges in interpretability, and the lack of reliable uncertainty assessment, especially in extrapolation beyond the training data.[31] Integrating physics-based constraints and relations as prior knowledge into the ML models can significantly enhance the interpretability of ML methods.[41] To overcome these pitfalls,

https://doi.org/10.1021/acs.jced.4c00071
J. Chem. Eng. Data XXXX, XXX, XXX−XXX

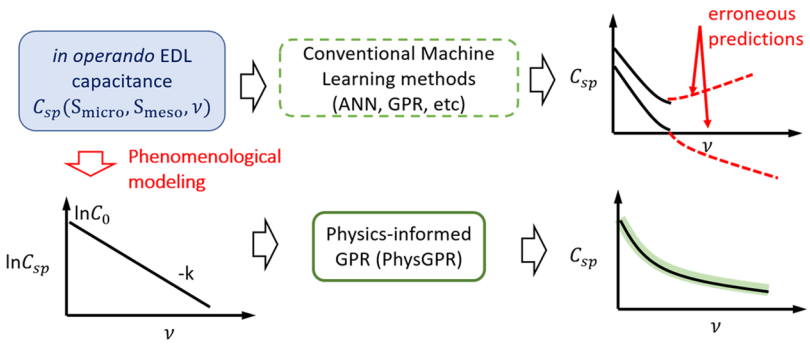

Figure 1. Physics-informed Gaussian process regression (PhysGPR) of the experimental data for the capacitance of carbon electrodes.

we propose in this work a physics-informed Gaussian process regression (GPR) (PhysGPR) model for predicting the *in operando* capacitance of aqueous supercapacitors based on the properties of nitrogen- and/or oxygen-doped carbon electrodes. The input parameters include the surface composition, the micropore and mesopore surface areas of the electrode, and the type of electrolyte and the operation conditions, as represented by the charging−discharging scan rate used in the cyclic voltammetry measurements. A phenomenological model for the charging dynamics is used as prior knowledge to avoid unphysical predictions. In general, GPR methods provide a reliable uncertainty assessment of the model performance compared with alternative ML methods such as ANN, alongside excellent data efficiency and great accuracy. Its mean or trend part can be tuned based on prior knowledge, as demonstrated in the construction of PhysGPR later. Previously, the GPR methods have been applied to predict the optimized composition of rGO/ANF/CNT electrodes, effectively balancing different qualities.[42]

There are significant outcomes of this contribution. First, we introduce novel input parameters, such as the proportion of oxygen and nitrogen atoms and the type of electrolytes, for constructing the PhysGPR model. These parameters are independent of each other and can be manipulated separately with little or a controllable impact on the others. The optimal results can be achieved through materials synthesis. We do not select highly correlated parameters such as the pore volume and surface area of different pore sizes because they do not change independently. Second, we implement the robust estimation of the parameters in Gaussian processes, utilizing the jointly robust prior function and marginal posterior mode estimation[26,32,41] and constructing the group automatic relevance determination (gARD) kernel in order to produce meaningful and accurate prediction by solving problems ordinary GPR methods face. The performance of PhysGPR is significantly improved in these ways compared to that of the original PhysGPR used on pristine carbon in our previous work.[36] The previous version faltered when applied to doped carbon due to the near-diagonal or near-singular correlation matrix, likely stemming from the sparseness of high-dimensional input parameters. Finally, harnessing the predictive capabilities of PhysGPR across various input variable ranges enables us to guide the experimental design of electrode materials, aiming for maximum capacitances. We compared the results with those predicted by the ANN models[43,44] and by conventional GPR with different settings. Furthermore, we tested different ways to train the PhysGPR model by considering either individual electrolyte types or different electrolytes together.

2. MODELS AND METHODS

In this section, we explain the preparation of the data set and mathematical details for the construction of physics-informed Gaussian process regression (PhysGPR) to predict the overall capacitance and power density of N/O-codoped carbon electrodes. Schematically, Figure 1 shows the training flowchart for PhysGPR in comparison with that for conventional ML methods. While the latter utilize experimental data directly, PhysGPR begins with a physics model that can be used to analyze the experimental results. In the present work, a phenomenological model is adopted for representing the dependence of the capacitance on the charging−discharging rate (here, the cyclic voltammetry scan rate). The physical model is then integrated into GPR with prior knowledge within a supervised ML algorithm. The model parameters are normalized and served as the input for the GPR training. The incorporation of the physical model allows us to avoid erroneous predictions that may otherwise occur in conventional ML methods.

All ML models and sensitivity analysis methods are available from packages kernlab, RobustGaSP, sensitivity, and DiceKriging of R programming language available from CRAN.[31,45−47] The optimization of the capacitor behavior was performed by using the "*optim*" function from R Stats packages. The default optimization method (Nelder and Meas) was employed, with multiple initial points to enhance robustness and accuracy. The technical details of the conventional GPR method, jointly robust (JR) prior, posterior mode estimation, and sensitivity analysis can be found in the Supporting Information (SI).

2.1. Data Collection. The experimental data for training our ML models were collected from the literature, and the formulas for obtaining the processed data are introduced in Table S2.[26,48−67] While there have been numerous investigations on the capacitance of heteroatom-doped carbons in aqueous electrolytes, only a limited number have provided the detailed structure parameters and the surface chemical composition. The capacitance data employed in this study were acquired through measurements conducted in three-electrode cell configurations, all within the same potential window range of 1 V. The three-electrode measurements provide more precise control over potential and current than two-electrode measurements.

The experimental data encompass two types of electrolytes, namely, 6 M KOH and 1 M H_2SO_4 aqueous solutions, which are widely utilized as basic and acidic electrolytes in supercapacitor research. In training the ML models, the electrolyte type is represented by a dummy variable: 0 means 6 M KOH and 1 means 1 M H_2SO_4. All measurements were

https://doi.org/10.1021/acs.jced.4c00071
J. Chem. Eng. Data XXXX, XXX, XXX−XXX

carried out with electrodes prepared by loading 5 mg of the carbon material on a 1 cm × 1 cm plate. The charging−discharging rates were determined by the cyclic voltammetry scan rate in the range of 1 to 500 mV/s (most data are in the range of 5 to 200 mV/s). The electrodes were made of carbon materials doped with oxygen and/or nitrogen with no other heteroatom doping except for a trace amount of hydrogen.

The input parameters used in the ML models include the cyclic voltammetry scan rate, the type of electrolyte, the structure parameters including the surface areas of micropores and mesopores, and the chemical compositions of the electrode surfaces, including the ratio of the O atom and the N atom. As mentioned above, the type of electrolyte is described with a dummy variable in the ML models. The surface areas reported in the experiments were measured from BET fitting of the N_2 adsorption isotherms at 77 K. Similar features were used in our previous work for pristine carbon electrodes and other ML models. The BET surface area provides a reasonable estimate of the accessible area of hydrated ions because their diameters are similar to that of a N_2 molecule. The experimental data for the chemical compositions of carbon surfaces were obtained exclusively through X-ray photoelectron spectroscopy (XPS) measurements.[68] It should be noted that all capacitive processes occur on the electrode surface and are virtually unrelated to the bulk composition of the carbon electrodes.

Artificial zero capacitance points have been introduced into the data set for electrodes with zero micro- and mesopore surface areas. The addition of these boundary points improves the model performance because they compensate for the lack of experimental data for materials with low specific surface areas (SSA), which are of limited practical significance. While these materials may still exhibit some capacitance from the surface area of macropores, these values would be small and sensitive to the electrode shape, particle size, and packing geometry.[69]

Outlier detection was performed by comparing the Mahalanobis distance of all of the samples to the cutoff distance derived from the χ^2 distribution with a 0.95 confidence level. Any outliers, excluding the artificial zero capacitance points, are subsequently removed.

Table 2. Input and Output Parameters Used for Training Machine-Learning Models[a]

Input	Output
SA_{micro} (m^2/g)	
SA_{meso} (m^2/g)	
Scan rate (mV/s)	Specific capacitance (F/g)
Oxygen (at. %)	
Nitrogen (at. %)	
Electrolyte type (dummy variable)	

[a]SA means surface area.

2.2. Physically Informed GPR and Parameter Space.

Both experimental observations and theoretical models indicate that the overall capacitance decreases monotonically with increasing scan rate. The trend can be attributed to limitations in ion transfer rates within micropores, alongside constraints in charge transfer and ion desolvation rates related to pseudocapacitance.[70] Whereas sophisticated molecular models have been developed to describe the charging dynamics of EDL capacitors,[71,72] a quantitative prediction of pseudocapacitance remains a theoretical challenge. Here, we apply the PhysGPR model introduced in our previous work for predicting the overall capacitance of pristine carbons.[73] The physics-informed ML method offers simplicity in incorporating contributions due to different charging mechanisms, including pseudocapacitance. To avoid unphysical predictions, we use a semiempirical formula to correlate the specific capacitance as a function of the scan rate

$$C_{sp} = C_0 e^{-k\nu} \tag{1}$$

where C_0 represents the equilibrium capacitance of the electrode material, $k > 0$ is a characteristic rate constant, and ν is the charging−discharging rate (i.e., the scan rate of cyclic voltammetry). As shown in Figure S1, eq 1 accurately represents the experimental data concerning the scan rate dependence of capacitance.

In training our ML models, we use the natural logarithm of the specific capacitance as the response vector for data regression:[72]

$$y = \ln C_{sp} = \ln C_o - k\nu \tag{2}$$

To accommodate a large number of input parameters in the PhysGPR model, we introduce a new basis function, $H(X)$, which consists of two components for the mean:

$$H(X) = [\nu H_1(\mathbf{X}_{mat}), H_2(\mathbf{X}_{mat})] \tag{3}$$

In eq 3, $\mathbf{X}_{mat} = [S_{micro}, S_{meso}, \text{O\%}, \text{N\%}, \text{electrolyte}]$ is a matrix that encapsulates the most important features of the electrode material. This matrix is defined by the experimental data for the micropore surface area SA_{micro}, mesopore surface area SA_{meso}, oxygen and nitrogen doping ratios in atomic surface percentage compositions O at. % and N at. %, and a dummy variable indicating the electrolyte type. While $H_1(\mathbf{X}_{mat}) = [1, \mathbf{X}_{mat}]$ serves the linear basis for $\mathbf{X}_{mat}$, $H_2(\mathbf{X}_{mat}) = [1, \mathbf{X}_{mat}, \mathbf{X}_{mat2}]$ represents the "pure quadratic" basis for $\mathbf{X}_{mat}$, as defined in eqs S9 and S10. Because X_{mat2} represents the half-vectorization of the quadratic form of $\mathbf{X}_{mat}$, the PhysGPR model can be expressed as

$$\begin{aligned} y &= [\nu H_1(\mathbf{X}_{mat}), H_2(\mathbf{X}_{mat})][\beta_1, \beta_2] + z(\mathbf{X}_{mat}) + \varepsilon \\ &\equiv H(\mathbf{X})\beta + z(\mathbf{X}_{mat}) + \varepsilon \end{aligned} \tag{4}$$

where $\beta = [\beta_1, \beta_2]$ is a vector of the basis coefficients, $z(\mathbf{X}_{mat})$ follows a zero-mean Gaussian process, and $\varepsilon \approx N(0, \sigma^2)$ is independent zero-mean Gaussian noise with a standard deviation of σ. By incorporating the semiempirical formula for C_{sp} with GPR, we take the artificial zero surface area points as 0.041 F/g such that their standardized values remain consistent before and after natural logarithm transformation.

According to the GPR, the marginal distribution of the response vector y follows a multivariate normal distribution. Given a vector of observations, the predictive distribution also follows a normal distribution. Consequently, the predictive distribution of specific capacitance C_{sp} follows a log-normal distribution. The mean and standard deviation of the response value (RV) of the capacitance are given by

$$\widehat{C_{sp}} = e^{\hat{y} + (y_{sd}^2/2)} \tag{5}$$

$$\sigma(C_{sp}) = \sqrt{(e^{y_{sd}^2} - 1)}\, e^{\hat{y} + (y_{sd}^2/2)} \tag{6}$$

https://doi.org/10.1021/acs.jced.4c00071
J. Chem. Eng. Data XXXX, XXX, XXX−XXX

Table 3. Training Set Root Mean Square Error (RMSE), Cross-Validation Root Mean Square Error (CVRMSE), and Mean Absolute Percentage Error (MAPE) for Different ML Models[a]

ML method	Kernel/training function	Training RMSE	CVMAPE	CVRMSE
gARD-JR-PhysGPR	Matérn 3/2	26.62	14.33%	30.44
	Matérn 5/2	25.38	17.06%	38.25
	Radial basis function (RBF)	33.66	16.09%	35.21
ARD-JR-PhysGPR	Matérn 3/2	22.87	15.52%	33.26
	Matérn 5/2	23.06	21.78%	40.69
	RBF	24.96	30.52%	51.87
gARD-MLE-PhysGPR	Matérn 5/2	20.37	18.22%	38.63
ARD-MLE-PhysGPR	Matérn 5/2	26.11	20.14%	48.25
gARD-JR-ConvGPR	Matérn 5/2	15.87	8.25%	30.79
ARD-JR-ConvGPR	Matérn 3/2	17.09	13.75%	41.55
gARD-MLE -ConvGPR	RBF	12.83	9.12%	28.14
ARD-MLE -ConvGPR	rational quadratic kernel	14.47	10.01%	41.93
gARD-JR-PhysGPR for KOH	Matérn 5/2	36.03	11.6%	58.05
gARD-JR-PhysGPR for H_2SO_4	Matérn 3/2	24.35	7.03%	30.47
ANN	Bayesian regularization	35.00	84.63%	52.50
Standard deviation				123.34

[a]Here, gARD-MLE-PhysGPR and ARD-MLE-PhysGPR denote physics-informed Gaussian process regression (GPR) models utilizing group automatic relevance determination (gARD) and conventional ARD methods, respectively. All ML models were optimized using marginal posterior mode estimation with joint robustness (JR) prior to or with an ordinary maximum likelihood estimation (MLE). For comparison, also shown are the results from fitting with an artificial neural network (ANN) and conventional GPR (ConvGPR) methods and the single-electrolyte-type gARD-JR-PhysGPR model using the kernel with the best correlation.

$$RV(C_{sp}) = \frac{\sigma(C_{sp})}{E(C_{sp})} = \sqrt{(e^{y_{sd}^2} - 1)} \tag{7}$$

In the above equations, $\widehat{C_{sp}}$ represents the mean prediction of the specific capacitance, $\sigma(C_{sp})$ denotes the standard deviation, and $RV(C_{sp})$ is the relative standard deviation. These equations are derived from the fact that $\hat{y}$ and y_{sd} are the mean and standard deviation of $\ln(C_{sp})$ predicted by the GPR model.

Unlike our previous work for pristine carbon electrodes,[74] in this study, we do not use the automatic relevance determination (ARD) kernel or separable kernel to decouple the input parameters, as ARD models show clear evidence of overfitting, as discussed in the next section. Instead, we collectively calculate the length scale parameters of the input data with the same unit. This implies that all parameters remain coupled in the GPR models, including (i) the surface areas of micropores and mesopores (in units of m^2/g) and (ii) the surface chemical compositions of N and O atoms expressed as the atomic surface percentage compositions (in units of at. %). As demonstrated below, this treatment substantially reduces the sparseness of the input data, thereby leading to a significant improvement in the correlation between the ML predictions and experimental data.[36] The refined ML model is termed the group ARD PhysGPR (gARD-PhysGPR), distinguishing itself from our previous work that utilized the ARD kernels (ARD-PhysGPR). In gARD-PhysGPR, we employed the jointly robust (JR) prior for the range parameters and marginal posterior mode estimation from the RobustGaSP package. Posterior mode estimation enhances the robustness of the range parameters by avoiding the near-diagonal or near-singular correlation matrix[36,44,75,76] while the JR prior enables fast computation as an ordinary method such as the maximum likelihood estimation (MLE). The GPR models incorporating these techniques are marked as JR- (such as gARD-JR-PhysGPR), in contrast to the ordinary GPR implemented in the kernlab package using the maximum likelihood estimation (MLE), which is marked as MLE-. As will be discussed in the next section, MLE models exhibit an overly robust mean function, as evidenced by predicting an ellipse-shaped contour and a highly stable predictive interval.

In the GPR analysis conducted in this study, we tested the squared exponential kernel (also known as the Gaussian kernel or the radial basis function (RBF) kernel), Matérn 3/2 kernel, and Matérn 5/2 kernel. The exponential kernel was not considered in this work because it is not first-order differentiable and produces erratic predictions. Additionally, the rational quadratic kernel was not utilized because it was not supported in RobustGaSP. For all GPR models, the fitting parameters (including the kernel, the parameter space variance parameter σ, and the nugget variance ratio η) were optimized with the random-sampling k-fold cross validation method. In this study, we use a k value of 5 with 10 different repartitions. This choice of the k value is based on the loss-training data ratio relationship, as demonstrated in Figure S2, where an 80% training data set proves sufficient to optimize the test set RMSE. The overall capacitance for different electrode materials was predicted by the final models using the fitting parameters found in cross validation.[43] To evaluate the numerical performance of different ML models in correlating the experimental data, we used the cross-validation root-mean-square error (CVRMSE) as the loss function. This quantity and the CV mean absolute percentage error (MAPE) are calculated from

$$\text{CVRMSE} = \sqrt{\frac{\sum_{j=1}^{k}\sum_{i=1}^{n}(\widehat{C_{sp,CV_{ij}}} - u_i)^2}{nk}} \tag{8}$$

$$\text{CVMAPE} = \frac{\sum_{j=1}^{k}\sum_{i=1}^{n}\frac{(\widehat{C_{sp,CV_{ij}}} - u_i)}{u_i}}{nk} \times 100\% \tag{9}$$

where n and k are the number of data points and the number of repartitions in cross-validation, respectively, u_i denotes the experimental values of C_{sp}, and $\widehat{C_{sp,CV_{ij}}}$ represents the prediction

https://doi.org/10.1021/acs.jced.4c00071
J. Chem. Eng. Data XXXX, XXX, XXX−XXX

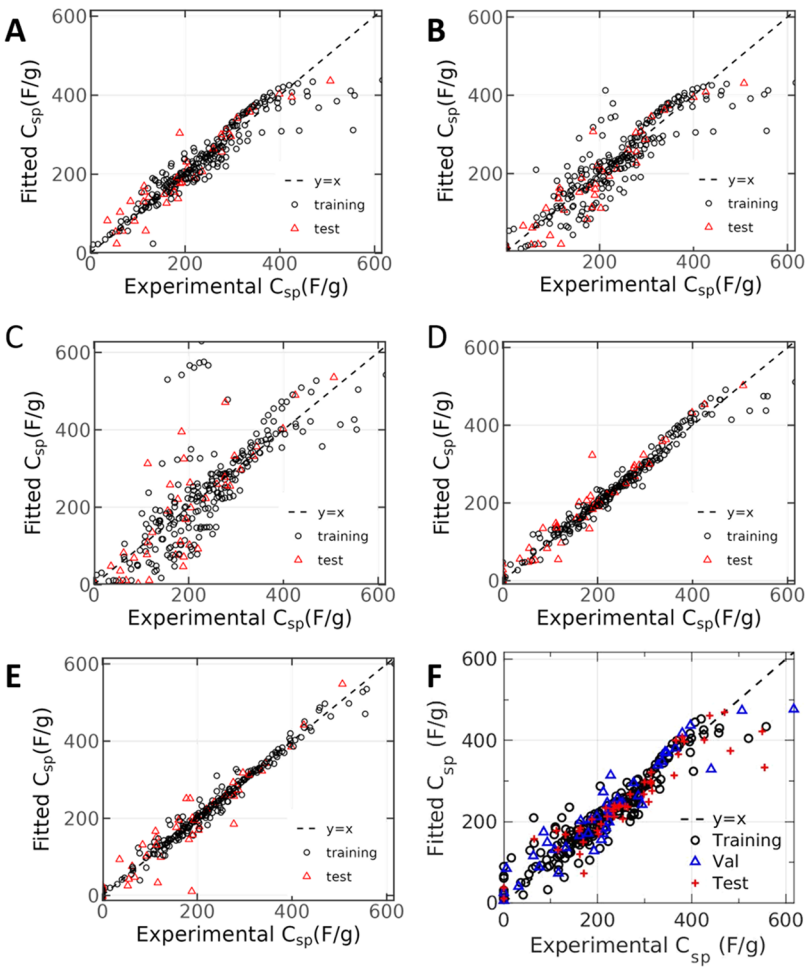

Figure 2. Correlation of experimental data for the specific capacitance of active carbons with different machine-learning (ML) models from one cross-validation test, with training:test = 8:2 for GPR models and training:validation:test = 8:1:1 for ANN. In each panel, the diagonal line represents the perfect correlation. (A) Group ARD physics-informed GPR with JR prior (gARD-JR-PhysGPR), marginal posterior mode estimation, and Matérn 3/2 kernel; (B) conventional ARD physics-informed GPR with JR prior (ARD-JR-PhysGPR), posterior mode estimation, and Matérn 3/2 kernel; (C) conventional ARD physics-informed GPR (ARD-MLE-PhysGPR) with maximum likelihood estimation (MLE) and Matérn 5/2 kernel; (D) gARD conventional GPR with JR prior (gARD-JR-ConvGPR), posterior mode estimation, and squared exponential kernel; (E) conventional GPR (ARD-MLE-ConvGPR) with pure quadratic basis and ARD rational quadratic kernel; and (F) artificial neural network (ANN).

for the test set in the *j*th repartition of the *k*-fold cross-validation.

3. RESULTS AND DISCUSSION

3.1. Model Evaluation. In this section, we first discuss the cross-validation correlation of gARD PhysGPR models with experimental data to access their prediction capabilities. We will compare the results with those obtained from the conventional GPR, PhysGPR with ARD kernels (all input parameters decoupled), and the artificial neural network (ANN) reported in our previous work. The fitting hyper-parameters were optimized by 5-fold cross validation (CV) with 10 repartitions (80% training, 20% test, trained 5 × 10 = 50 times). Table 3 summarizes the training and cross-validation error measured by CVRMSE for different ML models as well as the training set RMSE and CV mean absolute percentage error (MAPE).

Figure 2 illustrates the correlations of the experimental data with different ML models. In comparison with our previous work for pristine carbon electrodes, all ML models, except convGPR, exhibit improved fitting of the specific capacitance. This improvement is likely due to the increased number of data points and more input parameters. All kinds of PhysGPR and convGPR (JR or MLE) provide a good correlation of the experimental data for the specific capacitance, with different accuracies. Among various ML methods tested in this work, convGPR with the ARD rational quadratic kernel yields the lowest predictive error (CVRMSE = 28.14). However, as illustrated in Figure 3, both ANN and convGPR exhibit the unphysical prediction of capacitance increasing with the scan rate, resembling the behavior observed in pristine carbon electrodes. Consequently, these models may not always be suitable for accurate capacitance predictions. For all of the Phys-GPR models, using joint robust (JR) prior and posterior mode estimation reduces the cross-validation predictive error. Similarly, in most of the convGPR models, the improved robustness of the range parameters increases the model stability and accuracy for test set predictions.

Table 3 shows that all types of PhysGPR models tested in this study can correlate the experimental capacitance data better than ANN (CVRMSE = 52.50). Among various PhysGPR models, gARD-JR-PhysGPR with the Matérn 3/2

https://doi.org/10.1021/acs.jced.4c00071
J. Chem. Eng. Data XXXX, XXX, XXX−XXX

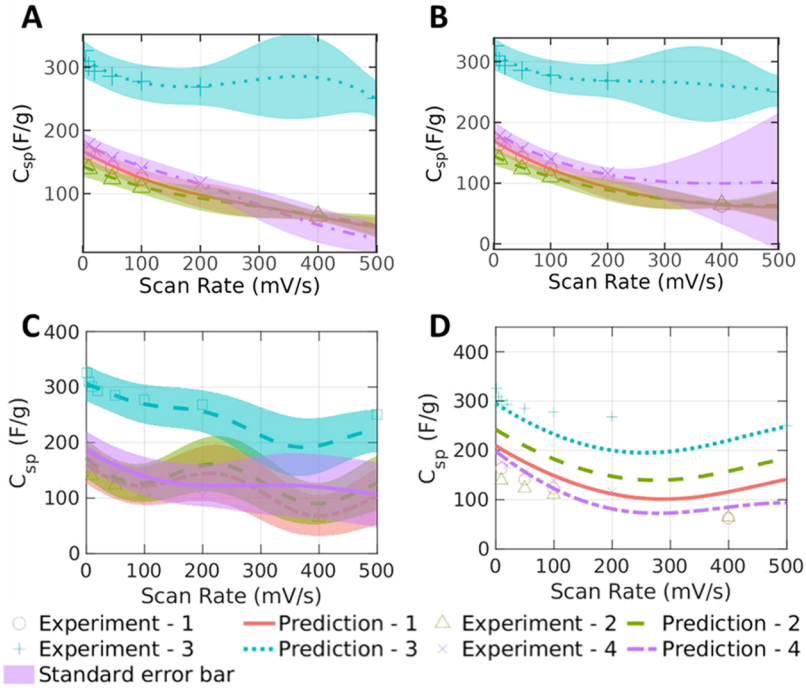

Figure 3. Specific capacitance (C_{sp}) versus the scan rate (ν) predicted by different machine-learning methods: (A) group ARD, jointly robust (JR) prior, posterior mode estimation physics-informed GPR (gARD-JR-PhysGPR) with Matérn 3/2 kernel; (B) automatic relevance determination (ARD) physics-informed GPR with Matérn 5/2 kernel; (C) conventional GPR with pure quadratic basis and ARD rational quadratic kernel; and (D) artificial neural network (ANN). The lines show the predicted mean value, while the shadow shows the standard deviation predicted by GPR. The input parameters for the electrode material are sample 1: SA_{micro} = 429 m^2/g, SA_{meso} = 118 m^2/g, O and N = 0 at. %, 6 M KOH electrolyte; sample 2: SA_{micro} = 173 m^2/g, SA_{meso} = 994 m^2/g, O = 5.23 at. % N = 3.69 at. %, 6 M KOH electrolyte; sample 3: SA_{micro} = 1347 m^2/g, SA_{meso} = 84 m^2/g, O = 13.86 at. %, N = 0 at. %, 1 M H_2SO_4 electrolyte; sample 4: SA_{micro} = 1167 m^2/g, SA_{meso} = 330 m^2/g, O = 9.25 at. %, N = 6.9 at. %, 1 M H_2SO_4 electrolyte.

kernel achieves the best performance (CVRMSE= 30.44). Coupling the input parameters with the same units improves the cross-validation (CV) correlation of the ML models compared to ARD-JR-PhysGPR (ARD Matérn 5/2, CVRMSE= 33.26), where all input parameters are decoupled. The reduced correlation accuracy may be attributed to the ARD kernel using many parameters (parameter space length scale), which increases data sparseness and results in overfitting. The fitted length parameter in the mesopore direction becomes too small for ARD models, resulting in significant frustration in that direction and unrealistically large predictions (Figure S7). Separate gARD-JR-PhysGPR models were developed for different electrolyte types. In comparison with the gARD-JR-PhysGPR model trained with all data, the single-electrolyte-type model yields similar correlation for samples with 1 M H_2SO_4 electrolyte (CVRMSE = 30.47). However, its performance is much worse for samples with 6 M KOH electrolyte (CVRMSE = 58.05). All ML models predict the artificial zero surface area−zero capacitance data points better than similar models for the pristine carbon electrodes.[44] The enhanced performance could be ascribed to the amplified influence of artificial points, stemming from the sparseness of the input data set induced by the higher dimensionality of the input parameter space.

As demonstrated in our previous work,[45] the direct application of ML models to correlate experimental data may result in problematic predictions of the capacitance for certain electrode materials. For example, Figure 3 shows that both ANN and convGPR models predict an upsurge in capacitance with the scan rate in the high-scan-rate region. The PhysGPR models circumvent the unphysical predictions because of the use of prior knowledge about the scan-rate dependence of the capacitance. PhysGPR shows significantly improved performance in the high-scan-rate region, making it the preferred choice for predicting the capacitance of doped carbon materials in the subsequent analyses. Additionally, the Gaussian process methods allow for the calculation of predictive standard deviation alongside the prediction mean, providing an uncertainty measurement. The comparison between ordinary ML models (using MLE) and posterior mode estimation with the JR prior underscores the importance of robustness in estimating the range parameter, which is crucial for avoiding near-diagonal or near-singular issues in these calculations.

Table S1 compares the capacitance prediction performance of our model and previously developed models from the literature.[22,34,38,77,78] Because of the choice of experimentally adjustable input parameters and the use of prior knowledge to avoid overfitting, our developed models do not outperform all previous models, and the accuracy of our results is comparable to that of other models with a reasonable number of input parameters.

3.2. Effect of Chemical Compositions and Structure Parameters. To comprehend the impact of heteroatom doping on the capacitive behavior of carbon electrodes, we conducted sensitivity analysis (SA) by computing the main effect and total effect Sobol indices of the trained ML model on all input parameters. The specifics of the SA methods are provided in the SI. We assumed that the input parameters are independent of each other and follow a uniform distribution

https://doi.org/10.1021/acs.jced.4c00071
J. Chem. Eng. Data XXXX, XXX, XXX−XXX

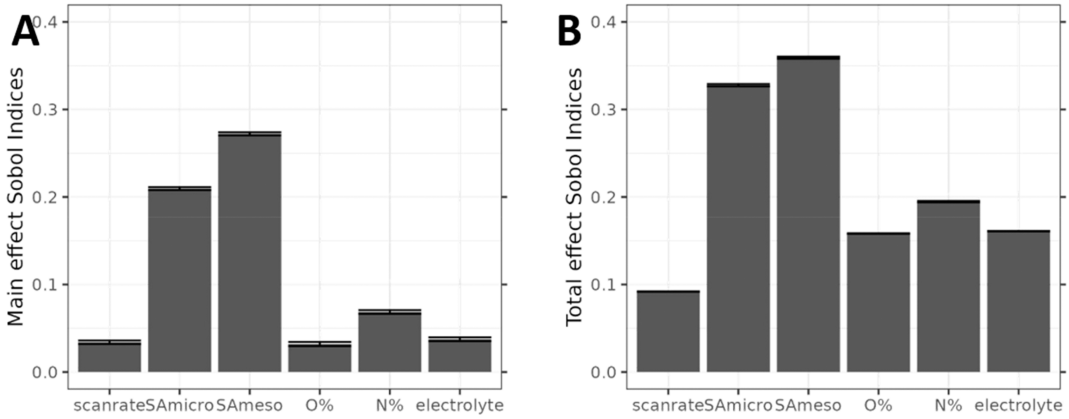

Figure 4. (A) Main effect and (B) total effect Sobol indices of the gARD-JR-PhysGPR model with the error bar showing the standard deviation.

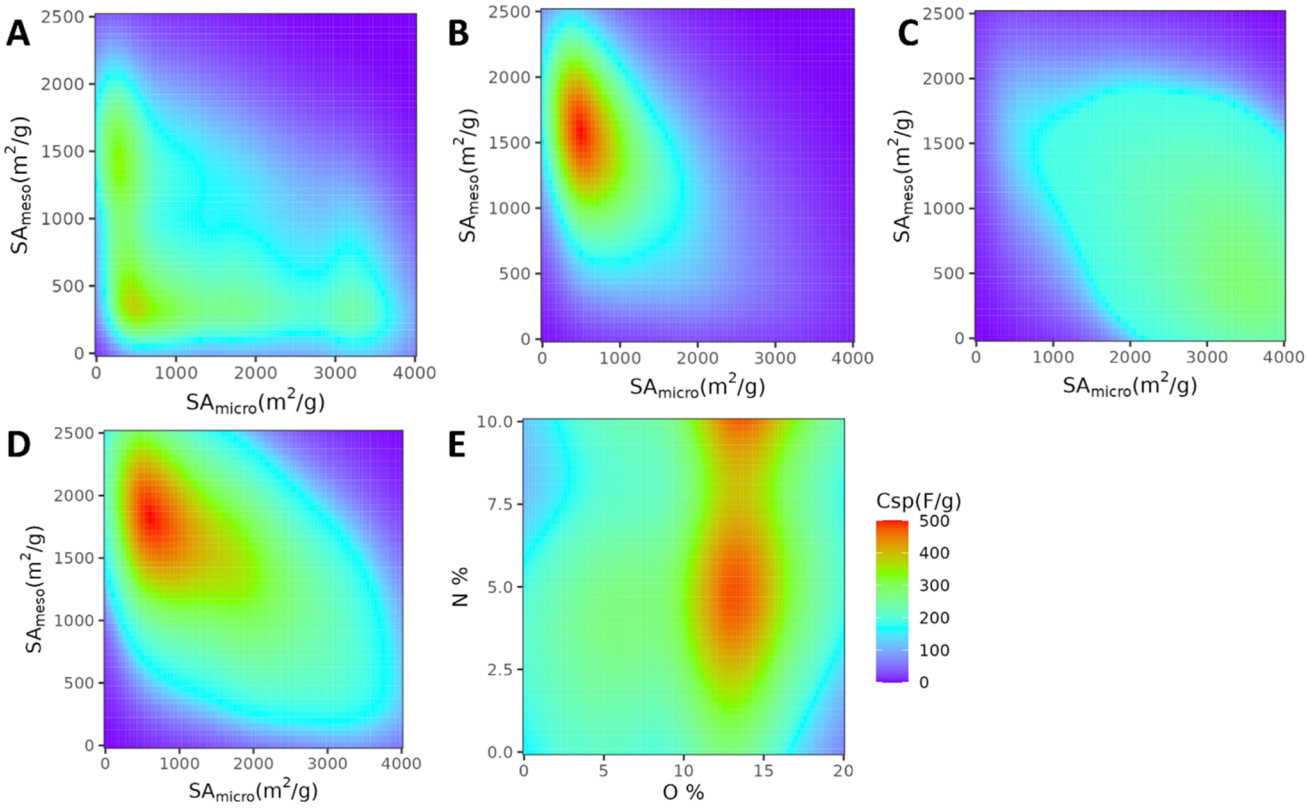

Figure 5. Specific capacitance versus the surface areas of micro- and mesopores of carbon electrodes predicted by gARD-JR-PhysGPR. (A) Pristine carbon, (B) single-doped carbon with N = 14.1 at. %, (C) single-doped carbon with O = 3.7 at. %, (D) codoped carbon with O = 13.3 at. % and N = 4.8 at. %, and (E) capacitance versus doping composition at SA_{micro} = 619 m^2/g and SA_{meso} = 1973 m^2/g. In all cases, the capacitance corresponds to 6 M KOH aqueous electrolyte at a scan rate of 1 mV/s.

with the same mean and standard deviation as for the training samples. From the main effect Sobol indices, we observed that the micropore surface area and mesopore surface area are the primary parameters influencing the overall capacitance. Additionally, the total effect Sobol indices were found to be significantly higher than the main effect indices for every parameter, indicating strong interactions between different parameters.

Then ML models were employed to explore the variation of specific capacitance with the structure parameters at a low scan rate (1 mV/s). The electrode materials considered in this study include pristine carbon, active carbon with single heteroatom doping, and active carbon with mixed doping of oxygen and nitrogen at different chemical compositions.

Figures 5 and 6 present the capacitance predicted by gARD-JR-PhysGPR for carbon electrodes in 1 M H_2SO_4 and 6 M KOH electrolytes, respectively. In these figures, each panel displays the capacitance as a function of two variables, and the chemical composition of the electrode is described by the atomic percent of N/O doping (e.g., 20 at. % oxygen means 20% of the surface atoms are oxygen atoms). The input variables of the prediction are selected within the ranges of SA_{micro} < 4000 m^2/g, SA_{meso} < 2500 m^2/s, O ratio < 20%, and N ratio < 10%. These values are chosen based on the experimental data set. Further extrapolation is problematic for

https://doi.org/10.1021/acs.jced.4c00071
J. Chem. Eng. Data XXXX, XXX, XXX−XXX

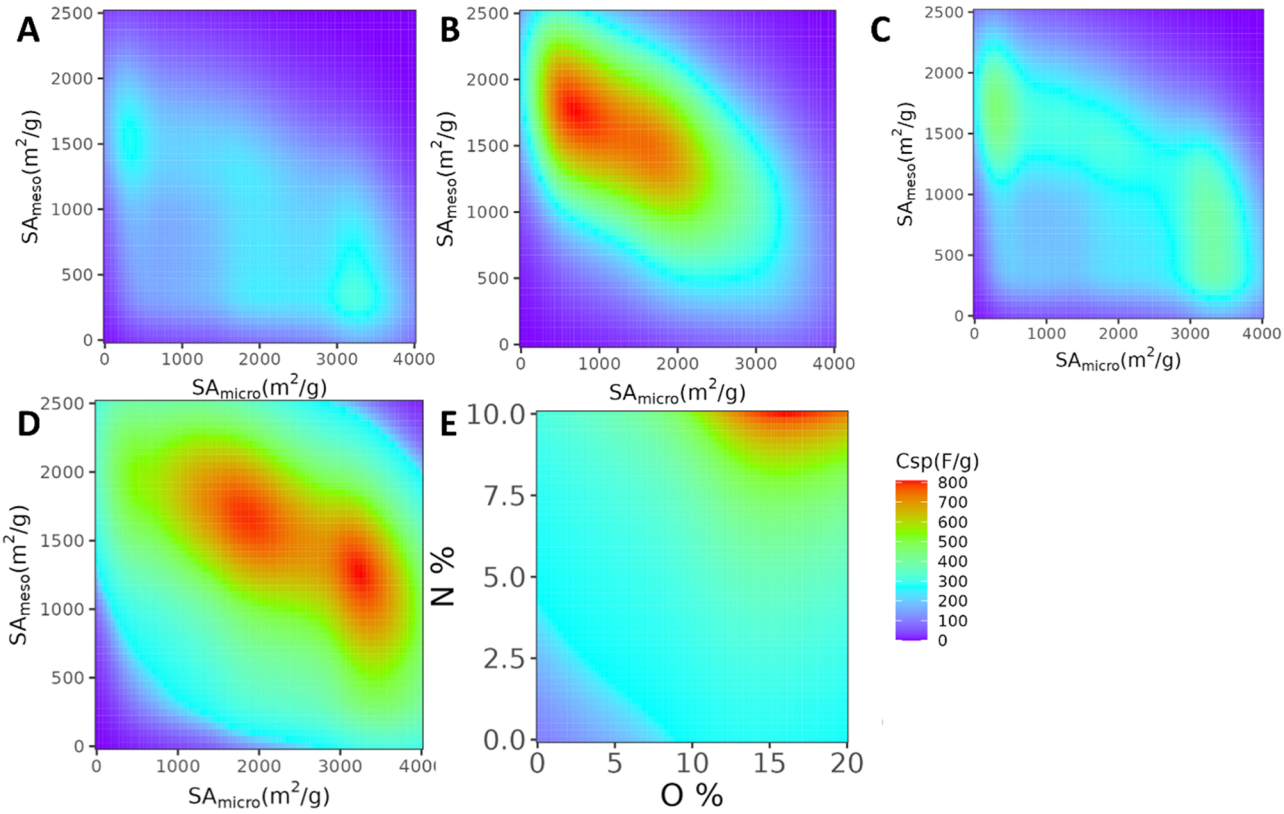

Figure 6. Capacitance vs surface areas of micropores and mesopores of carbon electrodes predicted by gARD-JR-PhysGPR. (A) Pristine carbon, (B) single-doped carbon with N = 8.0 at. %, (C) single-doped carbon with O = 20 at. %, (D) codoped carbon with O = 17.6 at. % and N = 10.0 at. %, and (E) capacitance versus doping composition at SA_{micro} = 1704 m^2/g and SA_{meso} = 1737 m^2/g. In all cases, the electrolyte is a 1 M H_2SO_4 aqueous solution, and the scan rate is fixed at 1 mV/s.

the ML models. The predicted capacitance refers to the capacitor material properties shown at the cross section in the direction of the structural parameters, SA_{micro} and SA_{meso} (4D and 5D), or chemical compositions, O% and N% (4E and 5E), at the position of the optimized material in different electrolytes.

Figure 6E shows that, for the single-doped carbon materials in 1 M H_2SO_4 aqueous solution, the O doping enhances the performance within the range of less than O = 20 at. %. In 6 M KOH solution, however, the capacitance begins to decrease at 13 at. % O doping, as illustrated in Figure 5E. The single N doping to the carbon electrode shows different effects in different electrolytes, as shown in Figures 5E and 6E. In 6 M KOH electrolyte, the ML model predicts a peak in specific capacitance at about N = 4.4 at. %. Conversely, in the acid solution, the capacitance increases with the N composition. Furthermore, the increase in capacitance due to doping is much stronger in the acidic electrolyte than in the alkaline electrolyte. In the former case, the maximum capacitance of N-doped carbon reaches 546 F/g, whereas under the alkaline condition, it is only 240 F/g.

Multiple configurations are possible for N doping on carbon materials, including pyrrolic nitrogen (N-5), pyridinic nitrogen (N-6), quaternary nitrogen (N-Q), and pyridinic oxide (N-X), with different effects on the capacitance.[36] N-X does not exist in N-doped carbon without oxygen. Previous experiments and theoretical investigations show that both N-5 and N-6 nitrogen doping would increase the capacitance by their contributions to pseudocapacitance, especially in an acidic electrolyte.[21,80] Figure 7 presents three possible photon-participating redox

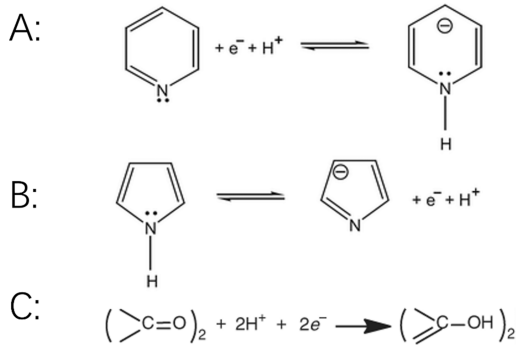

Figure 7. Possible redox reactions on N/O-doped carbon with pseudocapacitance effects.[36,79] (A) Pyridinic nitrogen (N-6), (B) pyrrolic nitrogen (N-5), and (C) quinone oxygen.

reactions. While N-5 is electrochemically more active than N-6, the latter has a redox reaction potential window larger than 1 V in a basic electrolyte. On the other hand, N-Q doping does not make any significant contribution to pseudocapacitance; its effect is limited to a slight increase in the EDL capacitance, primarily through the improvement of the electronic conductivity of the electrode material. The three kinds of N doping (N-5, N-6, and N-Q) can occur simultaneously during the material synthesis. The N-Q ratio rises in high N-doped materials, leading to the observed peak in capacitance.

Figures 5 and 6 elucidate how the N/O-codoped carbon electrodes exhibit distinct capacitive behaviors in different electrolyte solutions. For N-doped carbon materials, increasing

https://doi.org/10.1021/acs.jced.4c00071
J. Chem. Eng. Data XXXX, XXX, XXX−XXX

Table 4. Summary of Optimal Carbon Electrodes in 6 M KOH Electrolyte Predicted by Different ML Models in Comparison to the Best Material Identified in the Experiment

Optimization method	Properties of the optimized electrode				C_{sp} (F/g) at 5 mV/s		
	SA_{micro} (m^2/g)	SA_{meso} (m^2/g)	O at. %	N at. %	Source[b]	ANN[c]	Phys-GPR[a,c]
Experiment	327	1280	6.8	4.8	309.5	292	312
ANN	1400	1000	11.3	9.0	570	/	491
PhysGPR[a]	691	1973	13.3	4.8	568	301	/

[a]gARD-JR-PhysGPR is shown as PhysGPR. [b]Optimized specific capacitance. [c]ML predictions with alternative inputs.

Table 5. Same as for Table 3 but for the 1 M H_2SO4 Electrolyte

Optimization method	Properties of the optimized electrode				C_{sp} (F/g) at 5 mV/s		
	SA_{micro} (m^2/g)	SA_{meso} (m^2/g)	O at. %	N at. %	Source	ANN	Phys-GPR
Experiment	3650	826	11.78	1.56	610	583	617
ANN	1710	1050	20	2.3	692	/	673
PhysGPR	1704	1737	17.6	10	769	501	/

oxygen doping reduces the capacitance in both acidic and alkaline electrolytes when the oxygen content is beyond O = 12−16 at. %. The potential reason lies in the formation of N-X instead of N-6 in N/O-codoped carbon materials, which provides much less pseudocapacitance because its redox potential is higher than the experimental potential window of 1 V. A comparison of different panels of Figures 5 and 6 illustrating the specific capacitance versus the structure parameters (viz., micropore and mesopore surface areas) suggests that in an alkaline electrolyte heteroatom doping shifts the maximum capacitance to a higher mesopore surface area. Additionally, oxygen doping significantly improves the performance in materials with high mesopore surface area but worsens in those with high micropore surface area. The trend may be attributed to the increased surface wettability and thus higher ion accessibility of the micropores. By contrast, in an acidic electrolyte, oxygen doping shifts the maximum capacitance to a higher micropore surface area while nitrogen doping shifts the peak capacitance to a higher overall surface area and a slightly higher micropore surface area. These trends align with the physical mechanism of proton-participating redox pseudocapacitance.

We conclude this subsection by emphasizing the importance of incorporating the jointly robust (JR) prior to accurately capture the capacitive behavior using the Gaussian process model. To elucidate the effect of JR prior, we compared the results from gARD-MLE-PhysGPR and gARD-JR-PhysGPR predictions. As shown in Figure S8, the reference prior (ARD-MLE-PhysGPR) yields only one capacitance peak when the micropore and mesopore surface areas vary at different doping compositions, forming an ellipse-shaped contour. This result seems unrealistic and indicative of too strong a mean function in GPR. In theory, the variation in capacitance with respect to surface area should not be symmetric and will vary with chemical composition, owing to different charging mechanisms. Posterior mode estimation avoids the near-diagonal or near-singular correlation matrix and ensures the effectiveness of the parameter estimation, and the JR prior accelerates the decay of the tail of the kernel function compared to the reference prior, thereby reducing the range parameter of the inert inputs and long-range correlations.[30,81]

3.3. Capacitor Performance under Fast Charging−Discharging Conditions. In the preceding subsection, we discuss the interplay between pore structure and doping composition of carbon electrodes, unraveling their impact on the capacitance of aqueous supercapacitors. This exploration was conducted under a low scan rate, a regime closely aligned with the equilibrium condition and reflective of the maximum energy density. In practical applications, the performance of supercapacitors is often assessed under rapid charging and discharging conditions. In this subsection, we explore the influence of the pore structure and doping composition of carbon electrodes on the capacitance at higher scan rates. The results predicted by our ML model are shown in Figures S3−S6. The cross-sectional figures are similar to those in Figures 4 and 5 but at higher scan rates. The relative standard deviation (rSD) serves as an indicator of the uncertainty in GPR predictions. In comparison to the MLE models, the posterior mode estimation with the JR prior provides distinct uncertainty assessments for their predictions at various points. The relative predictive intervals of MLE models are highly stable, nearly fixed at rSD = 65% (Figure S9). This stability suggests potential overly robust mean function in the ordinary MLE GPR models, likely resulting from strong long-range correlation induced by the large kernel parameter length scale and a nearly diagonal correlation matrix. The reduced long-range correlation from the JR prior contributes to an effective uncertainty assessment.

In the KOH electrolyte, the specific capacitance drops more rapidly for materials with a high micropore surface area, whereas it remains little changed under high scan rates for materials with a high mesopore−low micropore surface area. In the acidic electrolyte, the specific capacitance declines with the rising scan rate, and the trend is not sensitive to chemical composition. In this case, the reduction in specific capacitance at high scan rate is relatively small compared to that for pristine carbons[23,44] or for the same electrodes in the KOH electrolyte solution (Figure 4). The probable reason is that pseudocapacitance dominates the performance of doped carbons in the acidic electrolyte. As a result, the limiting factor for the charging−discharging rate is similar for most carbon materials with the same doping composition. In the alkaline electrolyte, the ML model predicts that the retention rate of capacitance with scan rate is the highest for materials with 12−15% O and 10% N. The optimized condition is not observed in the acid electrolyte because the proton transfer process is much faster between doped sites and the solution under the acidic condition.

3.4. Optimizing Capacitive Performance with the ML Model. With the quantitative correlations between the

https://doi.org/10.1021/acs.jced.4c00071
J. Chem. Eng. Data XXXX, XXX, XXX−XXX

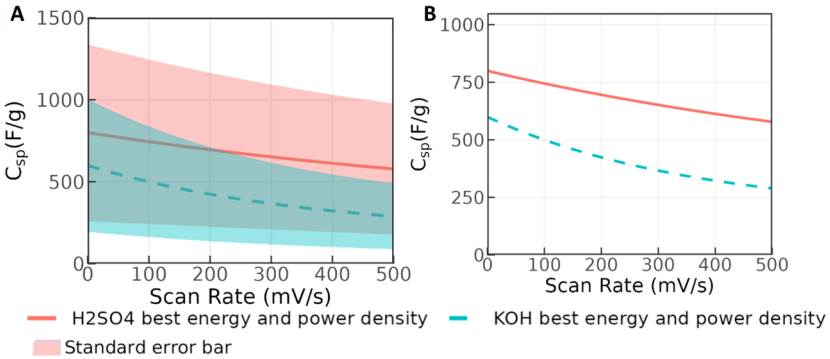

Figure 8. Specific capacitance versus scan rate predicted by the gARD-JR-PhysGPR model for nitrogen- and oxygen-codoped carbon electrodes that yield the highest capacitance at 1 and 200 mV/s scan rates in two different electrolytes. (A) Figure with error bar predicted by gARD-JR-PhysGPR. (B) Figure without error bar for clearance. The properties of the electrode materials are listed in Tables 4 and 5

material properties and specific capacitance derived from the gARD-JR-PhysGPR model, we can now explore the optimal structural parameters and doping compositions of carbon electrodes under different electrolyte conditions. In both acid and alkaline electrolytes, the optimal materials remain the same at scan rates of 1 and 200 mV/s, as illustrated in Figures S3–S6. An ultrahigh capacitance of 769 F/g can be achieved in H_2SO_4 at a scan rate of 1 mV/s. The characteristics of the optimized electrodes predicted by the gARD-JR-PhysGPR model are shown in Tables 4 and 5, in comparison with the optimized results by ANN and the best materials identified in the experiment. Figure 7 shows the specific capacitance versus the scan rate for the top materials predicted by the gARD-JR-PhysGPR model.

As anticipated, both ANN and gARD-JR-PhysGPR predict specific capacitance close to the experimental values for the optimized materials identified by experiment, demonstrating the robustness of these ML models. In the case of a 6 M KOH electrolyte solution, the two ML models also yield a similar value for the maximum specific capacitance (568 vs 570 F/g). However, the best electrode material predicted by the gARD-JR-PhysGPR model has a much higher mesopore surface area (1973 vs 1000 m^2/g) yet a smaller micropore surface area (691 vs 1400 m^2/g). It should be noted that the optimal material identified by ANN falls in the region where it predicts an unphysical increase in the capacitance with the scan rate. As depicted in Figure S10A, ANN predicts erroneous capacitive behavior in the high mesopore–low micropore surface area region, even at low to moderate scan rates. In a 1 M H_2SO_4 solution, the maximum specific capacitance predicted by gARD-JR-PhysGPR (769 F/g) is much higher than that predicted by ANN (692 F/g). The discrepancy likely arises from the fact that ANN systemically underestimates the capacitance at low scan rate in the high mesopore surface area region. Figure S10B illustrates that the unphysical increase in capacitance with the scan rate is most pronounced under the conditions where gARD-JR-PhysGPR predicts a maximum capacitance.

Figure 8 illustrates the variation of specific capacitance versus scan rate predicted by the gARD-JR-PhysGPR model for the electrode materials that yield the maximum capacitance. In the alkaline electrolyte, the optimized material is within the range of high retention rate with a high mesopore surface area and a 13% oxygen doping rate. In the acid electrolyte, the retention rate is not significantly impacted by the structural parameters.

3.5. Energy Storage Performance Comparison by the Ragone Plot.

To provide further insights into the performance of supercapacitors with optimal electrode materials, we prepared a Ragone plot as commonly used to compare the energy density and power density of different energy storage devices. Figure 9 is constructed based on the *in operando* capacitance of all N/O-codoped carbon materials in the parameter ranges of $S_{micro} < 4000$ m^2/g, $S_{meso} < 2500$ m^2/g, O-doped ratio < 20 at. %, and N-doped ratio < 10 at. % with a scan rate of 5 mV/s $\leq \nu \leq$ 100 mV/s. The results are predicted by the gARD-JR-GPR model and compared with those predicted by the ANN model for N/O-doped carbon electrodes.[45] Figure 9 also shows the energy density and power density of other energy storage devices such as batteries and conventional capacitors.[32] We observe that the maximum energy density predicted by gARD-JR-PhysGPR is slightly larger than that from the ANN prediction, while the ANN predicts a much higher power density. The red stars highlight the best energy density and power density for the optimal electrodes that are identified from the capacitance at scan rates of 1 and 200 mV/s, respectively.

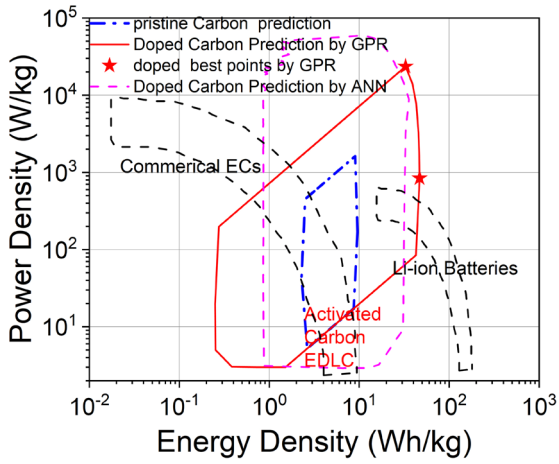

Figure 9. Ragone plot for aqueous supercapacitors consisting of nitrogen/oxygen-codoped carbon electrodes in 6 M KOH or 1 M H_2SO_4 electrolyte solution. The red solid line is predicted by the gARD-PhysGPR, the violet dashed line is the prediction of ANN, and the blue dashed line corresponds to that for pristine carbon electrodes. The red stars highlight the maximum energy density and power density, both obtained in the 1 M H_2SO_4 electrolyte.

https://doi.org/10.1021/acs.jced.4c00071
J. Chem. Eng. Data XXXX, XXX, XXX−XXX

The gARD-JR-PhysGPR model predicts that the optimized electrode structure has a micropore surface area of SA_{micro} = 1704 m^2/g and a mesopore surface area of SA_{meso} = 1737 m^2/g. These numbers may be compared with the best experimental samples with SA_{micro} = 3650 m^2/g and SA_{meso} = 820 m^2/g,[36] indicating a preference for synthesizing materials with a higher mesopore surface area but a lower micropore surface area. Among previously synthesized materials, those with a high mesopore surface area (>1000 m^2/g) typically exhibit relatively low micropore surface areas, with the highest recorded value being less than 620 m^2/g, thereby limiting their performance. According to our ML model, enhanced performance can be achieved by increasing the mesopore surface area while maintaining the micropore surface area at a relatively high level, around approximately 1500 m^2/g. Additionally, the ML model predicts that a higher capacitance can be attained by increasing the level of nitrogen doping.

Multiple strategies can be explored for synthesizing carbon materials with a high surface area through the activation of biomass or synthetic polymers. Materials with a high total surface area can often be achieved by chemical activation with KOH or $ZnCl_2$. While most chemical activation methods produce predominantly micropores, mesopores can be introduced in different ways, ranging from hard or soft templating to nontemplating methods such as simultaneous physical and chemical activation to enlarge micropores.[26,31,82] Hard templating means that the mesoporosity properties are introduced by nanocasting techniques using inorganic templates, such as mesoporous silica and zeolites. This method can reach a total surface area of 3840 m^2/g, with a relatively high mesopore surface area ratio (S_{meso} can reach 940 m^2/g). Soft templating refers to the adoption of ordered mesoporous frameworks that can be achieved by the cooperative assembly of amphiphilic molecules or block copolymers. Materials produced by soft templating tend to exhibit a highly ordered pore structure, albeit with a trade-off in their total surface area owing to a low micropore surface area. Nontemplating strategies are usually used to improve the mesopore surface area of active carbon from natural sources. Templating and nontemplating methods can be combined to reach higher mesopore surface area and volume at the cost of the ordered structure from the template. Meanwhile, heteroatom doping can be achieved by adding an element source in the synthesis steps, such as using a heteroatom-rich polymer as the carbon source or a separate nitrogen precursor, using postchemical treatment of carbon materials through an oxidation reaction, thermal polymerization, and replacement reactions, or using chemical vapor deposition.[16] The best material in the experiment is produced by the nontemplating treatment of a soft-templated material with cross-linked polymer produced by a poly(ethylene oxide)-*b*-poly(propylene oxide)-*b*-poly(ethylene oxide) (PEO-PPO-PEO)/phloroglucinol system as its carbon source and precursor with a nitrogen cross-linker.[83] Highly N/O-codoped porous carbon can be synthesized by activating a cross-linked polymer with a nitrogen precursor such as sodium amide, with a very high micropore surface area and a high mesopore surface area.[84] Applying the colloid-templated methods while synthesizing the cross-linked polymer is a possible route to improving the mesopore surface area for the porous carbon material further, while no templating methods such as additional physical activation can be used to transform a micropore into a mesopore.[16] Combining these methods may prove instrumental in achieving the optimal materials predicted by our ML models for capacitive energy storage.

4. CONCLUSIONS

We extended the PhysGPR model reported in our previous work for correlating the capacitive behavior of the pristine carbon supercapacitors to N/O-codoped carbon electrodes. A fixed-unit-relevance kernel was introduced to improve the model performance and reduce the likelihood of overfitting the sparse data. We demonstrated that the physics-informed ML model eliminates unphysical predictions that conventional GPR and ANN might encounter when fitting the capacitance versus scan rate curves. Quantitative correlations were established between the capacitive behaviors and a combination of structural information and surface chemical composition, in good agreement with the experimental data. This work demonstrates that incorporating physical knowledge into the learning algorithm can yield more meaningful and accurate predictions.

After incorporating capacitance data for carbon electrodes in a 1 M H_2SO_4 aqueous electrolyte, we observed that N/O-codoped carbon can achieve a higher capacitance under acidic conditions owing to the pH-related pseudocapacitance of pyrrolic nitrogen and pyridinic nitrogen groups. Among various forms of PhysGPR models, gARD-JR-PhysGPR with a Matérn 3/2 kernel provides the best correlation of the experimental data. Sensitivity analysis by the calculation of Sobol indices shows that the mesopore and micropore areas made more of a contribution to the capacitive behavior, with a strong correlation between different properties. The gARD-JR-PhysGPR model predicts that the specific capacitance of a N/O-codoped carbon can be optimized with an O-doping ratio of about 13 at. % and a high N-doping ratio, a micropore surface area of SA_{micro} = 1704 m^2/g, and a mesopore surface area of SA_{meso} = 1737 m^2/g. The preferred structure parameters of the doped carbon materials are different from those of the pristine carbons. High surface areas of both mesopores and micropores are preferred, but the performance of doped materials can be further optimized with medium to high micropore surface areas, consistent with the predictions of physics-based models of higher wettability of carbon electrodes and pore accessibility by ions.

In comparison with existing experimental results, the ML model predicts that materials with a higher mesopore surface area and a lower micropore surface area would be preferable for enhancing the capacitive performance of carbon electrodes in aqueous electrolytes. Meanwhile, the surface chemical compositions can be optimized by increasing the N-doping ratio with a comparable O ratio. The optimal material predicted by the ML model could potentially be synthesized by employing a more nitrogen-rich precursor in the soft template method, combining soft and hard templating to increase the mesopore surface area, or utilizing post-treatment methods to enhance the nitrogen doping ratio.

While conventional GPR methods offer uncertainty quantification, the sparsity of input data in the increasing order of the input parameter space diminishes the relevance of such uncertainty assessments. This results in uncertainty levels that remain medium to high across the parameter space, casting doubt on their applicability for single-point predictions. By employing the JR prior and posterior mode estimation in RobustGaSP, our gARD-JR-PhysGPR model offers a meaningful prediction interval as an uncertainty assessment. This

https://doi.org/10.1021/acs.jced.4c00071
J. Chem. Eng. Data XXXX, XXX, XXX−XXX

method enhances the range parameter estimation and mitigates the long-range effects of the training data, contributing to a more accurate and reliable uncertainty prediction. In general, random sampling high-dimensional model representation (RS-HDMR) methods would be a valuable approach for addressing sparse data as they are designed to effectively handle high-dimensional spaces and offer insights into the relationships between input variables and model output. However, RS-HDMR does not perform well in this work due to the limited number of input parameters and the occurrence of strong correlations between different parameters.[26,85] The gARD-JR-PhysGPR model allows us to account for the synergetic effects of nitrogen and oxygen doping and identify the best codoped carbon materials with desirable structural and chemical properties.

■ ASSOCIATED CONTENT

Supporting Information

The Supporting Information is available free of charge at https://pubs.acs.org/doi/10.1021/acs.jced.4c00071.

Formulas for calculating capacitance; machine-learning methods used in this study, including Gaussian process regression (GPR), robust parameter estimation, and sensitivity analysis; and 10 supplementary figures referenced in the main text and the input data for training the machine learning models (PDF)

■ AUTHOR INFORMATION

Corresponding Author

Jianzhong Wu − *Department of Chemical and Environmental Engineering, University of California, Riverside, California 92521, United States*; orcid.org/0000-0002-4582-5941; Email: jwu@engr.ucr.edu

Authors

Runtong Pan − *Department of Chemical and Environmental Engineering, University of California, Riverside, California 92521, United States*

Mengyang Gu − *Department of Statistics and Applied Probability, University of California, Santa Barbara, California 93106, United States*

Complete contact information is available at: https://pubs.acs.org/10.1021/acs.jced.4c00071

Notes

The authors declare no competing financial interest.

■ ACKNOWLEDGMENTS

R.P. expresses gratitude for the experimental data generously shared by Dr. Tao Wang as well as for the insightful discussions that enriched this research. This work is financially supported by the NSF-DFG Lead Agency Activity in Chemistry and Transport in Confined Spaces (under grant no. NSF 1152 2234013). M.G. acknowledges partial support from the National Science foundation under award no. DMS-2053423.

■ REFERENCES

(1) Zhai, Z.; et al. A review of carbon materials for supercapacitors. *Mater. Des.* **2022**, *221*, 111017.

(2) Zhong, M. Z.; Zhang, M.; Li, X. F. Carbon nanomaterials and their composites for supercapacitors. *Carbon Energy* **2022**, *4* (5), 950−985.

(3) Berrueta, A.; et al. Supercapacitors: Electrical Characteristics, Modeling, Applications, and Future Trends. *Ieee Access* **2019**, *7*, 50869−50896.

(4) Cao, Y.; et al. Mechanisms of Porous Carbon-based Supercapacitors. *ChemNanoMat* **2021**, *7* (12), 1273−1290.

(5) Volfkovich, Y. M. Electrochemical Supercapacitors (a Review). *Russian Journal of Electrochemistry* **2021**, *57* (4), 311−347.

(6) Tundwal, A.; et al. Developments in conducting polymer-, metal oxide-, and carbon nanotube-based composite electrode materials for supercapacitors: a review. *RSC Adv.* **2024**, *14* (14), 9406−9439.

(7) Barbieri, O.; et al. Capacitance limits of high surface area activated carbons for double layer capacitors. *Carbon* **2005**, *43* (6), 1303−1310.

(8) Lee, G. J.; Pyun, S. I. Theoretical approach to ion penetration into pores with pore fractal characteristics during double-layer charging/discharging on a porous carbon electrode. *Langmuir* **2006**, *22* (25), 10659−65.

(9) Hasegawa, G.; et al. New Insights into the Relationship between Micropore Properties, Ionic Sizes, and Electric Double-Layer Capacitance in Monolithic Carbon Electrodes. *J. Phys. Chem. C* **2012**, *116* (50), 26197−26203.

(10) Vasilyev, O. A.; Kornyshev, A. A.; Kondrat, S. Connections Matter: On the Importance of Pore Percolation for Nanoporous Supercapacitors. *ACS Applied Energy Materials* **2019**, *2* (8), 5386−5390.

(11) Kondrat, S.; Vasilyev, O. A.; Kornyshev, A. A. Feeling Your Neighbors across the Walls: How Interpore Ionic Interactions Affect Capacitive Energy Storage. *J. Phys. Chem. Lett.* **2019**, *10* (16), 4523−4527.

(12) Feng, G.; Cummings, P. T. Supercapacitor Capacitance Exhibits Oscillatory Behavior as a Function of Nanopore Size. *J. Phys. Chem. Lett.* **2011**, *2* (22), 2859−2864.

(13) Kondrat, S.; et al. A superionic state in nano-porous double-layer capacitors: insights from Monte Carlo simulations. *Phys. Chem. Chem. Phys.* **2011**, *13* (23), 11359−66.

(14) Eliad, L.; et al. Ion sieving effects in the electrical double layer of porous carbon electrodes: Estimating effective ion size in electrolytic solutions. *J. Phys. Chem. B* **2001**, *105* (29), 6880−6887.

(15) Ji, S.; et al. A universal electrolyte formulation for the electrodeposition of pristine carbon and polypyrrole composites for supercapacitors. *ACS Appl. Mater. Interfaces* **2020**, *12* (11), 13386−13399.

(16) Gao, Y.; et al. Doping strategy, properties and application of heteroatom-doped ordered mesoporous carbon. *RSC Adv.* **2021**, *11* (10), 5361−5383.

(17) Raghi, K. R.; Sherin, D. R.; Manojkumar, T. K. Theory, Modelling, and Simulation in Supercapacitors. *Polymer Nanocomposites in Supercapacitors*; CRC Press, 2022; pp 221−235.

(18) Wen, J.; et al. Identification of the different contributions of pseudocapacitance and quantum capacitance and their electronic-structure-based intrinsic transport kinetics in electrode materials. *Chem. Phys. Lett.* **2021**, *775*, 138666.

(19) Wei, M. M.; Yang, X. P. Solution dependence of quantum capacitors of doped carbon nanotubes. *Surfaces and Interfaces* **2022**, *29*, 101730.

(20) Zhang, B.; et al. Computational screening toward quantum capacitance of transition-metals and vacancy doped/co-doped graphene as electrode of supercapacitors. *Electrochim. Acta* **2021**, *385*, 138432.

(21) Aderyani, S.; et al. Simulation of cyclic voltammetry in structural supercapacitors with pseudocapacitance behavior. *Electrochim. Acta* **2021**, *390*, 138822.

(22) Wickramaarachchi, K.; et al. Repurposing N-Doped Grape Marc for the Fabrication of Supercapacitors with Theoretical and Machine Learning Models. *Nanomaterials (Basel)* **2022**, *12* (11), 1847.

(23) Zhan, C.; et al. Enhancing graphene capacitance by nitrogen: effects of doping configuration and concentration. *Phys. Chem. Chem. Phys.* **2016**, *18* (6), 4668−74.

(24) Kaneko, K.; et al. Origin of Superhigh Surface-Area and Microcrystalline Graphitic Structures of Activated Carbons. *Carbon* **1992**, *30* (7), 1075−1088.

(25) Chae, H. K.; et al. A route to high surface area, porosity and inclusion of large molecules in crystals. *Nature* **2004**, *427* (6974), 523−7.

(26) Wang, T.; et al. Machine-learning-assisted material discovery of oxygen-rich highly porous carbon active materials for aqueous supercapacitors. *Nat. Commun.* **2023**, *14* (1), 4607.

(27) Naseri, F.; et al. Supercapacitor management system: A comprehensive review of modeling, estimation, balancing, and protection techniques. *Renewable and Sustainable Energy Reviews* **2022**, *155*, 111913.

(28) Zeng, L.; et al. Molecular dynamics simulations of electrochemical interfaces. *J. Chem. Phys.* **2023**, *159* (9), 091001.

(29) Jeanmairet, G.; Rotenberg, B.; Salanne, M. Microscopic simulations of electrochemical double-layer capacitors. *Chem. Rev.* **2022**, *122* (12), 10860−10898.

(30) Tian, K.; et al. Single-site pyrrolic-nitrogen-doped sp(2)-hybridized carbon materials and their pseudocapacitance. *Nat. Commun.* **2020**, *11* (1), 3884.

(31) Zhou, M.; Vassallo, A.; Wu, J. Data-Driven Approach to Understanding the In-Operando Performance of Heteroatom-Doped Carbon Electrodes. *ACS Applied Energy Materials* **2020**, *3* (6), 5993−6000.

(32) Zhou, M. S.; et al. Insights from machine learning of carbon electrodes for electric double layer capacitors. *Carbon* **2020**, *157*, 147−152.

(33) Sawant, V.; Deshmukh, R.; Awati, C. Machine learning techniques for prediction of capacitance and remaining useful life of supercapacitors: A comprehensive review. *Journal of Energy Chemistry* **2023**, *77*, 438−451.

(34) Saad, A. G.; et al. Data-driven machine learning approach for predicting the capacitance of graphene-based supercapacitor electrodes. *Journal of Energy Storage* **2022**, *55*, 105411.

(35) Jamaluddin, A.; et al. Applying machine learning to understand the properties of biomass carbon materials in supercapacitors. *Energy Reports* **2023**, *10*, 3125−3132.

(36) Pan, R.; Gu, M.; Wu, J. Physics-informed Gaussian process regression of in operando capacitance for carbon supercapacitors. *Energy Advances* **2023**, *2* (6), 843−853.

(37) Mishra, S.; et al. The impact of physicochemical features of carbon electrodes on the capacitive performance of supercapacitors: a machine learning approach. *Sci. Rep.* **2023**, *13* (1), 6494.

(38) Liu, P.; et al. An emerging machine learning strategy for the assisted-design of high-performance supercapacitor materials by mining the relationship between capacitance and structural features of porous carbon. *J. Electroanal. Chem.* **2021**, *899*, 115684.

(39) Nanda, S.; Ghosh, S.; Thomas, T. Machine learning aided cyclic stability prediction for supercapacitors. *J. Power Sources* **2022**, *546*, 231975.

(40) Jha, S.; et al. Data-driven predictive electrochemical behavior of lignin-based supercapacitors via machine learning. *Energy Fuels* **2022**, *36* (2), 1052−1062.

(41) Beckh, K.; et al. Explainable Machine Learning with Prior Knowledge: An Overview. *arXiv*, 2021, DOI: 10.48550/arXiv.2105.10172.

(42) Patel, A. G.; et al. Design of multifunctional supercapacitor electrodes using an informatics approach. *Molecular Systems Design & Engineering* **2019**, *4* (3), 654−663.

(43) Gu, M. Jointly Robust Prior for Gaussian Stochastic Process in Emulation, Calibration and Variable Selection. *Bayesian Analysis* **2018**, *14* (3), 857−885.

(44) Gu, M.; Wang, X.; James. Robust Gaussian Stochastic Process Emulation. *Ann. Statist.* **2018**, *46* (6A), 3038−3066.

(45) Gu, M. Y.; Palomo, J.; Berger, J. O. RobustGaSP: Robust Gaussian Stochastic Process Emulation in R. *R Journal* **2019**, *11* (1), 112−136.

(46) Marrel, A.; et al. Calculations of Sobol indices for the Gaussian process metamodel. *Reliability Engineering & System Safety* **2009**, *94* (3), 742−751.

(47) Srivastava, A.; Subramaniyan, A. K.; Wang, L. Analytical global sensitivity analysis with Gaussian processes. *AI EDAM* **2017**, *31* (3), 235−250.

(48) Deringer, V. L.; et al. Gaussian Process Regression for Materials and Molecules. *Chem. Rev.* **2021**, *121* (16), 10073−10141.

(49) Rasmussen, C. E. Gaussian Processes in Machine Learning. *Advanced Lectures on Machine Learning. ML 2003*; Bousquet, O. U.; von Luxburg, G., Rätsch, Eds.; Springer: Berlin, 2004; pp 63−71.

(50) Chen, X. Y.; et al. Nitrogen-Doped Porous Carbon Prepared from Urea Formaldehyde Resins by Template Carbonization Method for Supercapacitors. *Ind. Eng. Chem. Res.* **2013**, *52* (30), 10181−10188.

(51) Chen, X. Y.; et al. Nitrogen-doped porous carbon for supercapacitor with long-term electrochemical stability. *J. Power Sources* **2013**, *230*, 50−58.

(52) Hao, X.; et al. Bacterial-cellulose-derived interconnected meso-microporous carbon nanofiber networks as binder-free electrodes for high-performance supercapacitors. *J. Power Sources* **2017**, *352*, 34−41.

(53) Jiang, L.; et al. Construction of nitrogen-doped porous carbon buildings using interconnected ultra-small carbon nanosheets for ultra-high rate supercapacitors. *Journal of Materials Chemistry A* **2016**, *4* (29), 11388−11396.

(54) Li, Y.-T.; et al. Hierarchical porous active carbon from fallen leaves by synergy of K2CO3 and their supercapacitor performance. *J. Power Sources* **2015**, *299*, 519−528.

(55) Liu, W.; et al. Nitrogen-Doped Hierarchical Porous Carbon from Wheat Straw for Supercapacitors. *ACS Sustainable Chem. Eng.* **2018**, *6* (9), 11595−11605.

(56) Liu, Y.; et al. N−O−S Co-doped Hierarchical Porous Carbons Derived from Calcium Lignosulfonate for High-Performance Supercapacitors. *Energy Fuels* **2020**, *34* (3), 3909−3922.

(57) Ma, C.; et al. Sustainable recycling of waste polystyrene into hierarchical porous carbon nanosheets with potential applications in supercapacitors. *Nanotechnology* **2020**, *31* (3), No. 035402.

(58) Mu, J.; et al. Fishbone-derived N-doped hierarchical porous carbon as an electrode material for supercapacitor. *J. Alloys Compd.* **2020**, *832*, 154950.

(59) Song, Z.; et al. Synergistic design of a N, O co-doped honeycomb carbon electrode and an ionogel electrolyte enabling all-solid-state supercapacitors with an ultrahigh energy density. *Journal of Materials Chemistry A* **2019**, *7* (2), 816−826.

(60) Song, Z.; et al. Nitrogen-Enriched Hollow Porous Carbon Nanospheres with Tailored Morphology and Microstructure for All-Solid-State Symmetric Supercapacitors. *ACS Applied Energy Materials* **2018**, *1* (8), 4293−4303.

(61) Tan, J.; et al. Nitrogen-doped porous carbon derived from citric acid and urea with outstanding supercapacitance performance. *Electrochim. Acta* **2015**, *178*, 144−152.

(62) Tang, Q. F.; et al. Integrating Effect of Surface Modification of Microporous Carbon by Phosphorus/Oxygen as well as the Redox Additive of p-Aminophenol for High-Performance Supercapacitors. *Advanced Materials Interfaces* **2020**, *7* (7), 1901933.

(63) Wang, Y.; et al. Preparation of novel pigskin-derived carbon sheets and their low-temperature activation-induced high capacitive performance. *RSC Adv.* **2014**, *4* (85), 45318−45324.

(64) Wu, H.; et al. The effect of activation technology on the electrochemical performance of calcium carbide skeleton carbon. *J. Solid State Electrochem.* **2012**, *16* (9), 2941−2947.

(65) Xue, D.; et al. Template-Free, Self-Doped Approach to Porous Carbon Spheres with High N/O Contents for High-Performance Supercapacitors. *ACS Sustainable Chem. Eng.* **2019**, *7* (7), 7024−7034.

(66) Yang, W.; et al. Template-free synthesis of ultrathin porous carbon shell with excellent conductivity for high-rate supercapacitors. *Carbon* **2017**, *111*, 419−427.
(67) Zhang, D.; et al. Scalable synthesis of hierarchical macropore-rich activated carbon microspheres assembled by carbon nanoparticles for high rate performance supercapacitors. *J. Power Sources* **2017**, *342*, 363−370.
(68) Zhang, J.; et al. Preparation of activated carbon from waste Camellia oleifera shell for supercapacitor application. *J. Solid State Electrochem.* **2012**, *16* (6), 2179−2186.
(69) Zhou, X.; et al. Biomass based nitrogen-doped structure-tunable versatile porous carbon materials. *Journal of Materials Chemistry A* **2017**, *5* (25), 12958−12968.
(70) Zhu, D.; et al. A general strategy to synthesize high-level N-doped porous carbons via Schiff-base chemistry for supercapacitors. *Journal of Materials Chemistry A* **2018**, *6* (26), 12334−12343.
(71) Seredych, M.; et al. Surface functional groups of carbons and the effects of their chemical character, density and accessibility to ions on electrochemical performance. *Carbon* **2008**, *46* (11), 1475−1488.
(72) Pean, C.; et al. On the dynamics of charging in nanoporous carbon-based supercapacitors. *ACS Nano* **2014**, *8* (2), 1576−83.
(73) Compton, R. G.; Banks, C. E. *Understanding Voltammetry*; Imperial College Press: London, 2011.
(74) Wu, J. Understanding the Electric Double-Layer Structure, Capacitance, and Charging Dynamics. *Chem. Rev.* **2022**, *122* (12), 10821−10859.
(75) Aslyamov, T.; Sinkov, K.; Akhatov, I. Relation between Charging Times and Storage Properties of Nanoporous Super-capacitors. *Nanomaterials (Basel)* **2022**, *12* (4), 587.
(76) Manzhos, S.; Ihara, M. Advanced Machine Learning Methods for Learning from Sparse Data in High-Dimensional Spaces: A Perspective on Uses in the Upstream of Development of Novel Energy Technologies. *Physchem* **2022**, *2* (2), 72−95.
(77) Shariq, M.; et al. Machine learning models for prediction of electrochemical properties in supercapacitor electrodes using MXene and graphene nanoplatelets. *Chemical Engineering Journal* **2024**, *484*, 149502.
(78) Tawfik, W. Z.; et al. An artificial neural network model for capacitance prediction of porous carbon-based supercapacitor electro-des. *Journal of Energy Storage* **2023**, *73*, 108830.
(79) Zhang, P. Model Selection Via Multifold Cross-Validation. *Annals of Statistics* **1993**, *21* (1), 299−313.
(80) Gao, Z. Y.; et al. Graphene incorporated, N doped activated carbon as catalytic electrode in redox active electrolyte mediated supercapacitor. *J. Power Sources* **2017**, *337*, 25−35.
(81) Deng, Y.; et al. Review on recent advances in nitrogen-doped carbons: preparations and applications in supercapacitors. *Journal of Materials Chemistry A* **2016**, *4* (4), 1144−1173.
(82) Mathis, T. S.; et al. Energy Storage Data Reporting in Perspective-Guidelines for Interpreting the Performance of Electro-chemical Energy Storage Systems. *Adv. Energy Mater.* **2019**, *9* (39), 1902007.
(83) Benzigar, M. R.; et al. Recent advances in functionalized micro and mesoporous carbon materials: synthesis and applications. *Chem. Soc. Rev.* **2018**, *47* (8), 2680−2721.
(84) Liang, C.; Li, Z.; Dai, S. Mesoporous carbon materials: synthesis and modification. *Angew. Chem., Int. Ed. Engl.* **2008**, *47* (20), 3696−717.
(85) Ren, O.; et al. Random Sampling High Dimensional Model Representation Gaussian Process Regression (RS-HDMR-GPR) for representing multidimensional functions with machine-learned lower-dimensional terms allowing insight with a general method. *Computer Physics Communications* **2022**, *271*, 108220.

https://doi.org/10.1021/acs.jced.4c00071
J. Chem. Eng. Data XXXX, XXX, XXX−XXX